Light field camera all-in-focus image acquisition based on angular information

YINGCHUN WU[1], XING CHENG[1*], JIE LIANG[2], ANHONG WANG[1], XIANLING ZHAO[1]

[1]School of Electronic Information Engineering, Taiyuan University of Science and Technology,
 No. 66 Waliu Road, Taiyuan 030024, China

[2]School of Engineering Science, Simon Fraser University,
 8888 University Drive, Burnaby, BC, V5A 1S6, Canada

*Corresponding author: 1205406867@qq.com

Traditional light field all-in-focus image fusion algorithms are based on the digital refocusing technique. Multi-focused images converted from one single light field image are used to calculate the all-in-focus image and the light field spatial information is used to accomplish the sharpness evaluation. Analyzing the 4D light field from another perspective, an all-in-focus image fusion algorithm based on angular information is presented in this paper. In the proposed method, the 4D light field data are fused directly and a macro-pixel energy difference function based on angular information is established to accomplish the sharpness evaluation. Then the fused 4D data is guided by the dimension increased central sub-aperture image to obtain the refined 4D data. Finally, the all-in-focus image is calculated by integrating the refined 4D light field data. Experimental results show that the fused images calculated by the proposed method have higher visual quality. Quantitative evaluation results also demonstrate the performance of the proposed algorithm. With the light field angular information, the image feature-based index and human perception inspired index of the fused image are improved.

Keywords: all-in-focus image fusion, light field camera, spatial information, angular information, macro-pixel energy difference.

1. Introduction

Traditional all-in-focus image is obtained by fusing multiple local clear images which are captured by multiple exposures of one camera with changing focal length. The pixel -based or region-based image fusion algorithms are often used to evaluate the sharpness of the multi-focused images and the fusion rules are established by comparing the sharpness evaluation results [1, 2]. As the imaging geometry changing and mechanical shaking during the camera focusing [3], the imaging range and the imaging angle of different images captured at different times are changed and the image matching degree is declined, which eventually result in the high complexity of the image fusion algorithms. The micro-lens array based light field camera is developed from the

light field imaging theory and can calculate multiple highly matched refocused images from one single light field raw image by digital refocusing technique [4, 5], which has significant advantages in the all-in-focus image acquisition.

Generally, the traditional all-in-focus image calculation methods based on the light field camera include two steps which are digital refocusing and refocused image fusion [4–6]. In the digital refocusing, a 2D refocused image is obtained by a change of basis of the 4D light field data in the spatial domain and then double integrating the 4D data along the angular direction [4], or taking a 2D slice from the 4D light field in the frequency domain and then performing inverse Fourier transform on the 2D slice [5]. In the refocused image fusion, traditional image fusion algorithms can be directly used, which can be accomplished in the spatial domain or in the transformed domain [7–10]. The most commonly used image fusion methods include the Laplace operator evaluation (LOE) [11] algorithm, wavelet transform (WT) algorithm [12], principal component analysis (PCA) algorithm [13], guided filtering fusion (GFF) [14] algorithm, and boundary finding (BF) [2] algorithm, *etc*. In these image fusion algorithms, since the inputs are the 2D images obtained by integrating the 4D light field data along the angular direction, only the spatial information of the 4D light field is considered in the focus measure and the angular information is ignored.

In this paper, the 4D light field data is analyzed from another perspective, and an all-in-focus image fusion algorithm based on light field angular information is presented. The 4D light field data is directly fused in the proposed algorithm. The light field digital refocusing is split into two steps of change of basis and integration, then the 4D light field data fusion and guided filtering are added between the two steps. So the all-in-focus image is calculated in the digital refocusing process with the proposed method. In the 4D light field data fusion, a macro-pixel energy difference function based on angular information is established to evaluate the image sharpness, and then the fused 4D data is refined by the guided filtering of the central sub-aperture image.

2. Light field all-in-focus image calculation based on refocused images

The light field camera has the significant advantage of digital refocusing after the picture is taken. Therefore, based on the digital refocusing, multi-images focused at different depths can be calculated from one single light field raw image [4]. The all-in-focus image can be obtained by fusing multi-refocused images. According to the digital refocusing theory, multi-refocused images can be obtained by using the 4D light field data $L(x, y, u, v)$ which is decoded from the light field raw image [4, 5]:

$$I_n(x, y) = \frac{1}{\alpha_n^2 F^2} \iint L\left[\frac{1}{\alpha_n}x + \left(1 - \frac{1}{\alpha_n}\right)u, \frac{1}{\alpha_n}y + \left(1 - \frac{1}{\alpha_n}\right)v, u, v\right]\mathrm{d}u\mathrm{d}v \qquad (1)$$

where F denotes the distance between the main lens and the sensor plane of the light field camera, α_n is the refocusing parameter, and $\alpha_n F$ denotes the distance between the

main lens and the refocusing plane after refocusing. Letting $n = 1, 2, 3, ..., N$, the parameter α_n has N different values corresponding to N refocused images.

Based on the traditional multi-focus image fusion algorithms, the refocused image fusion can be accomplished in the spatial domain or in the transform domain. In the spatial-domain-based algorithms, the pixels, blocks, and regions are used as the sharpness evaluation units [15], and the weight map of each refocused image is calculated by comparing the sharpness degree of each unit [2, 13, 14]:

$$\omega_n(x, y) = \begin{cases} 1 & \text{if} \quad C_n(x, y) = \max\Big[C_1(x, y), C_2(x, y), ..., C_N(x, y) \Big] \\ 0 & \text{otherwise} \end{cases} \tag{2}$$

where $C_n(x, y)$ denotes the sharpness index value of the n-th refocused image $I_n(x, y)$, and max[·] denotes the maximum value of the sharpness index. The final fused image is obtained by weighted averaging of the refocused images and the corresponding weight maps:

$$F(x, y) = \sum_{n=1}^{N} \Big[\omega_n(x, y) \cdot I_n(x, y) \Big] \tag{3}$$

For the transform-domain-based algorithms, the feature matrices of the refocused images are calculated in a transform domain, then a fusion rule is established to calculate the fused feature matrix, and the final fused image is obtained by performing inverse transform of the fused matrix [12, 16]. Taking the basic wavelet transform based image fusion algorithm as an example, the high frequency coefficients and low frequency coefficients are extracted from the source images by using the wavelet transform. According to the fusion rule, the maximum values are selected from the high frequency coefficients and the mean values are calculated in the low frequency coefficients. For the fused high and low frequency coefficients inverse transforms are performed to obtain the final fused image [12].

3. All-in-focus image fusion based on 4D light field angular information

The light field digital refocusing technique and traditional multi-focus image fusion algorithm are combined directly in the traditional light field all-in-focus image fusion. Single light field raw image is converted to multi-refocused images with digital refocusing technique and then multi-refocused images are fused to obtain an all-in-focus image [6]. Since the multi-refocused images are obtained by double integration of the 4D light field data along the angular direction (u, v), only the spatial information (x, y) is preserved. Therefore, the spatial information (x, y) of the 4D light field is used to accomplish the sharpness evaluation and the sharpness variance of the integrated images caused by angular information is ignored. Focusing on this problem, an all-in-focus

image fusion algorithm based on light field angular information is proposed in this section. The digital refocusing process is decomposed, and the series of 4D light field data focused on different depths are obtained by basis change of the raw 4D data. The macro-pixel energy difference of the 4D data are calculated by using the angular information for sharpness evaluation to accomplish the 4D light field fusion, then the fused 4D data is refined by the guided filtering of the central sub-aperture image, and finally an all-in-focus image is obtained by integrating the refined 4D light field data.

3.1. Calculation of 4D light field matrices focused on different depths

In order to use the angular information (u, v) of the light field in establishing the 4D data fusion rule, the digital refocusing described in Eq. (1) is split into two steps: changing of the basis of the 4D light field $L(x, y, u, v)$ firstly and then double integrating the basis-changed light field to obtain the refocused images $I_n(x, y)$. Based on the above analysis, the Eq. (1) can be further expressed as [5]:

$$I_n(x, y) = \frac{1}{\alpha_n^2 F^2} L_2^4 \cdot B_{\alpha_n} \Big[L(x, y, u, v) \Big] \tag{4}$$

where $B_{\alpha_n}[\cdot]$ denotes the change of the basis operator and $L_2^4[\cdot]$ represents the double integration operator. The operators of basis change and double integration are defined as follows:

$$B_{\alpha_n} \Big[L(x, y, u, v) \Big] = L \Big([x, y, u, v] \cdot B_{\alpha_n} \Big) \tag{5}$$

$$L_2^4 \Big[L(x, y, u, v) \Big] = \iint L(x, y, u, v) \, du \, dv \tag{6}$$

where $[x, y, u, v]$ represents the row vector and B_{α_n} is a 4D change of basis matrix defined in Ref. [5].

According to Eq. (5), taking different α_n values, different 4D light field data corresponding to different focus depths can be obtained. The 4D light field $L_{\alpha_n}(x', y', u', v')$ at different focus depths can be expressed as

$$L_{\alpha_n}(x', y', u', v') = L \Big([x, y, u, v] \cdot B_{\alpha_n} \Big) \tag{7}$$

Compared with Eq. (1), the light field angular information is preserved in the 4D data calculated by Eq. (7). Sets of 4D light field data calculated in Eq. (7) are used for the 4D data fusion in this paper, and an all-in-focus image fusion based on angular information can be accomplished. To simplify the notation, $L_{\alpha_n}(x', y', u', v')$ are denoted as $L_{\alpha_n}(x, y, u, v)$ hereafter.

3.2. Angular information analysis and 4D light field data fusion

Supposing that the spatial resolution of 4D light field camera is $X \times Y$ and the angular resolution is $U \times V$, the 4D light field data visualization can be shown in Fig. 1. The co-
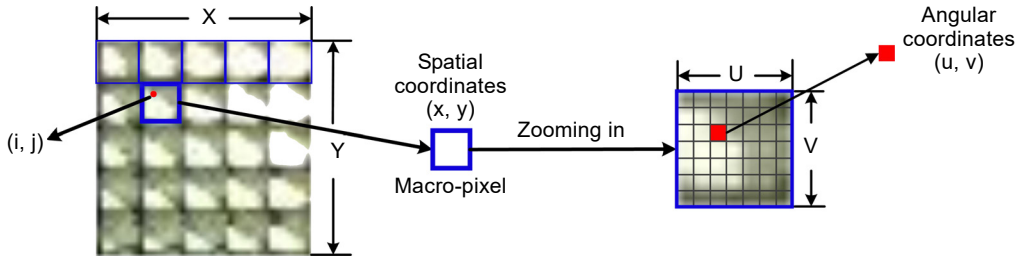
Fig. 1. The 2D visualization of the 4D light field data.

ordinate relationship between the 4D light field data $L(x, y, u, v)$ and the 2D visualized image $I(i, j)$ can be written as:

$$\begin{cases} i = Ux + u \\ j = Vy + v \end{cases} \tag{8}$$

According to Fig. 1, the significant feature of light field image is each "macro-pixel" corresponding to different micro-lens records of the angular information of the ray. In order to track the ray captured by each macro-pixel, the 4D light field $L(x, y, u, v)$ is simplified as 2D $L(x, u)$ and (x, u) is determined by the intercept of the ray with the micro-lens array plane and the main lens plane on the ray-space diagram [17], as shown in Fig. 2**a**. The micro-lens array plane is on the focal length of the main lens and the sensor plane is on the focal length of the micro-lens. The energy collected by the sensor plane is shown in Fig. 2**b**. Analyzing two points A and B in the space, A is on the cam-
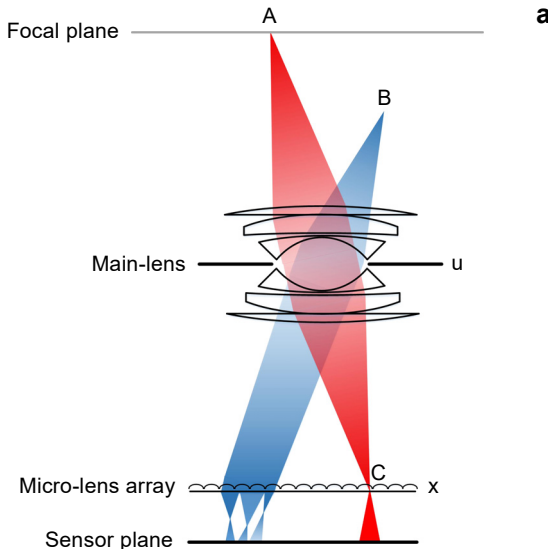

Fig. 2. Focus measure based on angular information: (**a**) the ray tracing of different object points, (**b**) the energy collected by the sensor plane, and (**c**) the angular difference when *x* is fixed.
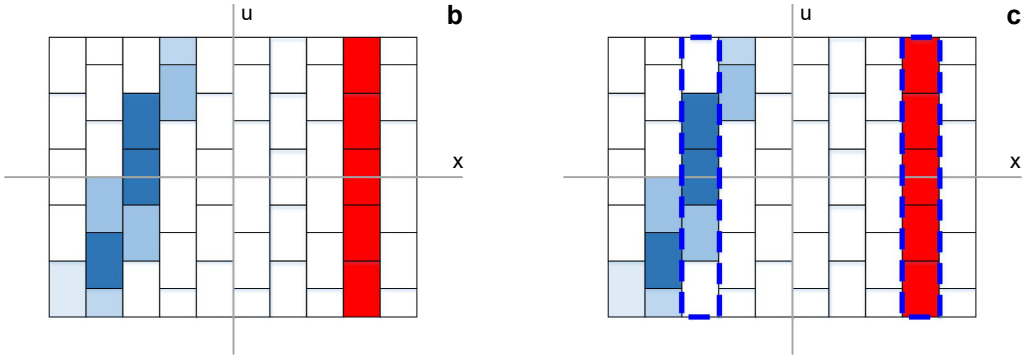
Fig. 2. Continued.

era's focal plane and B is out of the focal plane. Refracted by the main lens, the lights emitted from A converge on point C of a micro-lens and then convert to collimated light on the sensor plane. So the light radiation is uniform in the red region of Fig. 2**b**. In contrast, point B is out of the focal plane, and the light radiation is nonuniform in the blue region of Fig. 2**b**.

Fixing the coordinate x, the light radiation is nonuniform through direction on the sensor plane if the object point is out of the focal plane, otherwise the light radiation is uniform which can be analyzed from Fig. 2**c**. In the left-sided blue dotted rectangle of Fig. 2**c**, the colors of the pixels are different, which means that the light radiation is nonuniform. In contrast, in the right-sided blue dotted rectangle of Fig. 2**c**, the pixels are denoted with the same color, which means that the light radiation is uniform. Replacing the 2D $L(x, u)$ with 4D $L(x, y, u, v)$, when we fix the spatial coordinate (x, y), the corresponding light radiation region is defined as a macro-pixel in Fig. 1. So the energy difference caused by angular difference of the ray recorded by each macro-pixel can be used as a focus measure.

Based on the above analysis, a macro-pixel energy difference function is proposed in this paper. For each macro-pixel (x, y), the energy difference can be calculated by the following algorithm:

$$D_{\alpha_n}(x, y) = \sum_{u=1}^{U} \sum_{v=1}^{V} \left[L_{\alpha_n}(x, y, u, v) - L_{\alpha_n}\left(x, y, \frac{U+1}{2}, \frac{V+1}{2}\right) \right]^2 \tag{9}$$

where $L_{\alpha_n}(x, y, (U+1)/2, (V+1)/2)$ denotes the gray value of the central view point in the macro-pixel (x, y) of the light field $L_{\alpha_n}(x, y, u, v)$.

Moreover, a 4D light field fusion rule based on macro-pixel energy difference is established in this paper: for each macro-pixel, the smallest energy difference of all the 4D light field matrices is chosen to construct the fused 4D light field matrix. By scanning all the spatial coordinates (x, y) of the 4D light field, the weight matrices corresponding to different 4D light field matrices can be obtained:

$$W_{\alpha_n}(x, y, u, v) = \begin{cases} [1]_{U \times V} & \text{if } D_{\alpha_n}(x, y) = \min(D_{\alpha_1}(x, y), D_{\alpha_2}(x, y), ..., D_{\alpha_N}(x, y)) \\ [0]_{U \times V} & \text{otherwise} \end{cases}$$

(10)

where $[1]_{U \times V}$ denotes the all-one matrix of size $U \times V$, $[0]_{U \times V}$ denotes the all-zero matrix of size $U \times V$; min[·] denotes calculating the minimum, N denotes the number of 4D light field matrices to be fused. In Eq. (10), the sharpness indices $D_{\alpha_n}(x, y)$ are calculated based on the angular information of the light field. Smaller value of $D_{\alpha_n}(x, y)$ indicates the higher sharpness degree of the refocused, so the minimum is used in Eq. (10). The fused 4D light field matrix is calculated by weighted averaging of the weight matrices and the corresponding 4D light field matrices:

$$L_{\alpha_n}^F(x, y, u, v) = \sum_{n=1}^{N} W_{\alpha_n}(x, y, u, v) \cdot L_{\alpha_n}(x, y, u, v)$$

(11)

3.3. Fused 4D light field data guided filtering and projection

The macro-pixel energy difference in Eq. (9) is calculated through comparing the gray value of each pixel with the central view point. Based on Eq. (10) and Eq. (11), the macro-pixels with smallest energy difference are selected to construct the fused 4D light field matrix. So the gray value is smooth inside the macro-pixel and the edge is sharp between macro-pixels in the fused 4D light field matrix. If the macro-pixels can be further smoothed by the guided filtering which has the feature of edge-preserving smoothing, the fused 4D light field can be refined. The central sub-aperture image consisted of all the central view point in different macro-pixels can be used as the guidance image. The central sub-aperture image can be calculated as

$$I_c(x, y) = L(x, y, u, v)\Big|_{u = \frac{U+1}{2}, v = \frac{V+1}{2}}$$

(12)

Since the dimension of the guidance image is not matched with the input 4D data, the dimension increasing is performed on the 2D central sub-aperture image with the nearest neighbor interpolation algorithm:

$$L_c(x, y, u, v)\Big|_{u = [1 \sim U], v = [1 \sim V]} = I_c(x, y)$$

(13)

According to Eq. (13), each pixel in the central sub-aperture image is repeated to construct a macro-pixel in the guidance matrix $L_c(x, y, u, v)$.

The guided filter of the fused 4D light field data can be described as [18]:

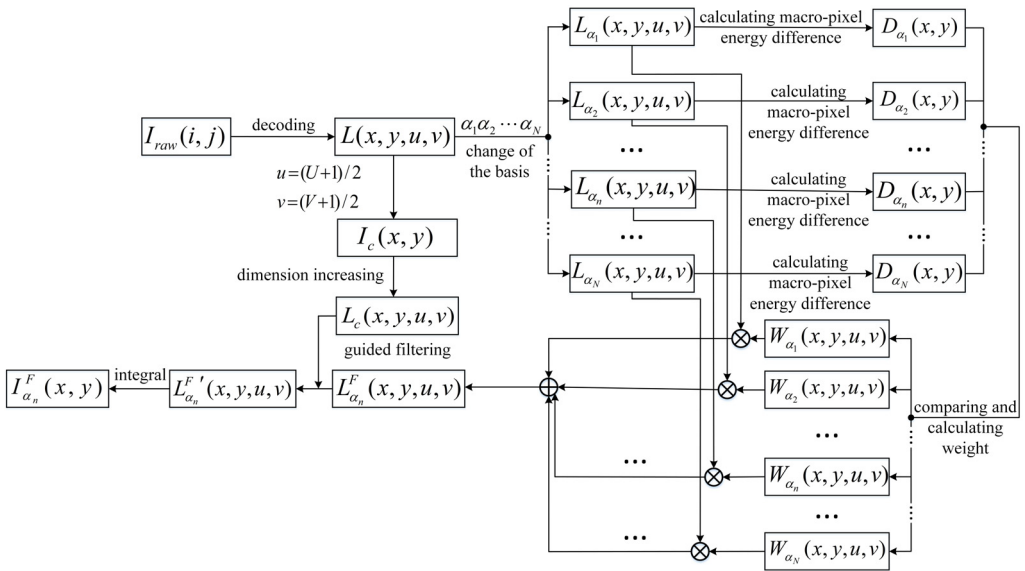$$O_i = a_k I_i + b_k, \quad \forall i \in \omega_k$$

(14)

Fig. 3. Flow chart of the proposed all-in-focus image fusion based on angular information.

where O represents the refined 4D data $L_{\alpha_n}^{F}{}'(x, y, u, v)$, I represents the dimension increased central sub-aperture image $L_c(x, y, u, v)$, and a_k and b_k are the coefficients which are related to the input 4D data $L_{\alpha_n}^{F}(x, y, u, v)$ and $L_c(x, y, u, v)$. The guided filter windows ω_k centered at different pixels k contain the pixel i.

Integrating the refined 4D light field matrix along the (u, v) direction, the final all-in-focus image is obtained:

$$I_{\alpha_n}^{F}(x, y) = \sum_{u=1}^{U} \sum_{v=1}^{V} L_{\alpha_n}^{F}{}'(x, y, u, v) \tag{15}$$

The flow chart of the proposed light field all-in-focus image fusion algorithm is shown in Fig. 3. The 4D light field matrix $L(x, y, u, v)$ is decoded from the raw light field image $I_{\text{raw}}(i, j)$. Changing the basis of 4D matrix $L(x, y, u, v)$, different 4D light field matrices $L_{\alpha_n}(x, y, u, v)$ corresponding to different focused depths can be achieved. Calculating the macro-pixel energy difference $D_{\alpha_n}(x, y)$ of all the 4D light field matrices $L_{\alpha_n}(x, y, u, v)$, the weight matrices $W_{\alpha_n}(x, y, u, v)$ can be obtained by comparing the values of $D_{\alpha_n}(x, y)$. The fused 4D light field $L_{\alpha_n}^{F}(x, y, u, v)$ is calculated by weighted average the 4D matrices $L_{\alpha_n}(x, y, u, v)$ with the weight matrices $W_{\alpha_n}(x, y, u, v)$, and then guided filtered by the central sub-aperture image $I_c(x, y)$ to obtain a refined 4D light field $L_{\alpha_n}^{F}{}'(x, y, u, v)$. Finally, the fused all-in-focus image of $L_{\alpha_n}^{F}(x, y)$ is got by double integration of the refined 4D light field $L_{\alpha_n}^{F}{}'(x, y, u, v)$.

4. Experiment results and analysis

In order to verify the feasibility of the proposed light field all-in-focus image fusion algorithm based on angular information, the dataset in Ref. [19] which is captured by the Lytro light field camera is used. The image *Dinosaur* is chosen to calculate the all-in-focus image. The number and value of α_n should be chosen firstly. N denotes the number of α_n. In theory, the larger N, the more images focused at different depths can be calculated, and a higher quality all-in-focus image can be obtained. However, considering the time complexity of the fusion algorithm, the smaller N is better when the fused all-in-focus image can satisfy the sharpness index. The value of α_n determines the focus region of the refocused image, so the value of α_n can be selected equidistantly in a reasonable range. The effective range of the α_n has been given in Ref. [4].

Three α_n are chosen in this part. When $\alpha_1 = 0.9$, $\alpha_2 = 10$, and $\alpha_3 = 200$, the 2D visualization of the 4D light field $L_{\alpha_1}(x, y, u, v)$, $L_{\alpha_2}(x, y, u, v)$, and $L_{\alpha_3}(x, y, u, v)$ are shown in Figs. 4a–4c, respectively. Figure 4d shows the 2D refocused image of raw 4D light field $L(x, y, u, v)$ and Fig. 4e shows the magnified red rectangles in Fig. 4d. Calculating and comparing the macro-pixel energy difference of Figs. 4a–4c, the corresponding weight matrices are shown in Figs. 4f–4h. It can be seen based on the angular information, the reasonable weight map can be calculated. The final fused all-in-focus image is shown in Fig. 4i. And the magnified red rectangles in Fig. 4i are shown in Fig. 4j.
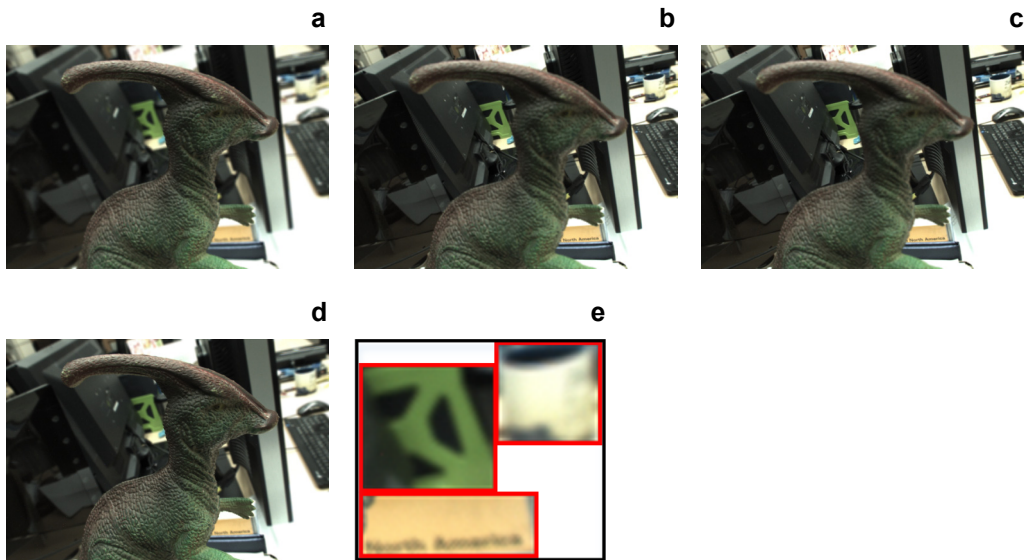

Fig. 4. Light field all-in-focus image fusion based on angular information. 2D visualization of the basis-changed 4D light field data at (**a**) $\alpha_1 = 0.9$, (**b**) $\alpha_2 = 10$, and (**c**) $\alpha_3 = 200$; (**d**) the 2D refocused image of raw 4D light field $L(x, y, u, v)$; (**e**) the magnified red rectangles in **d**; (**f**–**h**) the weight matrices of **a**–**c**, respectively; (**i**) all-in-focus image fused by the proposed algorithm; (**j**) the magnified red rectangles in **i**.
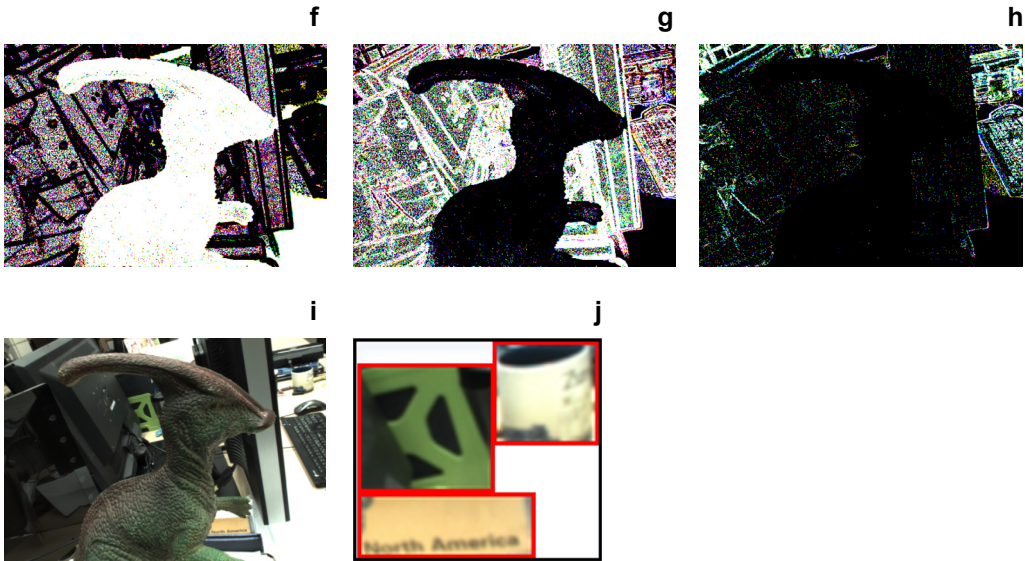
Fig. 4. Continued.

Comparing the magnified local regions in Fig. 4**e** and 4**j**, the sharpness is obviously improved in Fig. 4**i**, which demonstrates the feasibility of the proposed algorithm.

Moreover, another two images *Wheel* and *Buddha* in Ref. [19] are used as the test images to qualitatively and quantitatively evaluate the performance of the proposed algorithm, as shown in Figs. 5**a** and 6**a**. The LOE algorithm [11], WT algorithm [12], PCA algorithm [13], GFF algorithm [14], and BF algorithm [2] are used as the comparison algorithms to calculate the fused images. Adjusting the value of α_n, multi-refocused images can be obtained according to Eq. (1). To speed up the data processing, two refocused images whose focused regions are notably different are chosen as the source images to be fused with the comparison methods, as shown in (**b**) and (**c**) of Figs. 5 and 6, and the fused results are shown in (**d**–**h**) of Figs. 5 and 6. Choosing the same α_n, two basis-changed light field matrices can be calculated according to Eq. (9), and the final fused images obtained by the proposed algorithm are shown in Figs. 5**i** and 6**i**. The magnified local areas of the fused images of different algorithms are shown in (**j**) and (**k**) of Figs. 5 and 6. Comparing the sharpness degree of the magnified areas, the GFF algorithm, BF algorithm and the proposed algorithm perform better than that with the LOE algorithm, WT algorithm and PCA algorithm in general. In (**j**) and (**k**) of Figs. 5 and 6, the edge texture in the local regions (emphasized by the white dotted rectangles) calculated by the proposed algorithm are clearer than that of the other comparison algorithms, which indicates that the image visual effect of the proposed angular information based algorithm is better than that of the other spatial information based algorithms.

Considering the limitation of human vision, the qualitative evaluation may not reflect the fused image quality objectively, so the fused images are further quantitatively
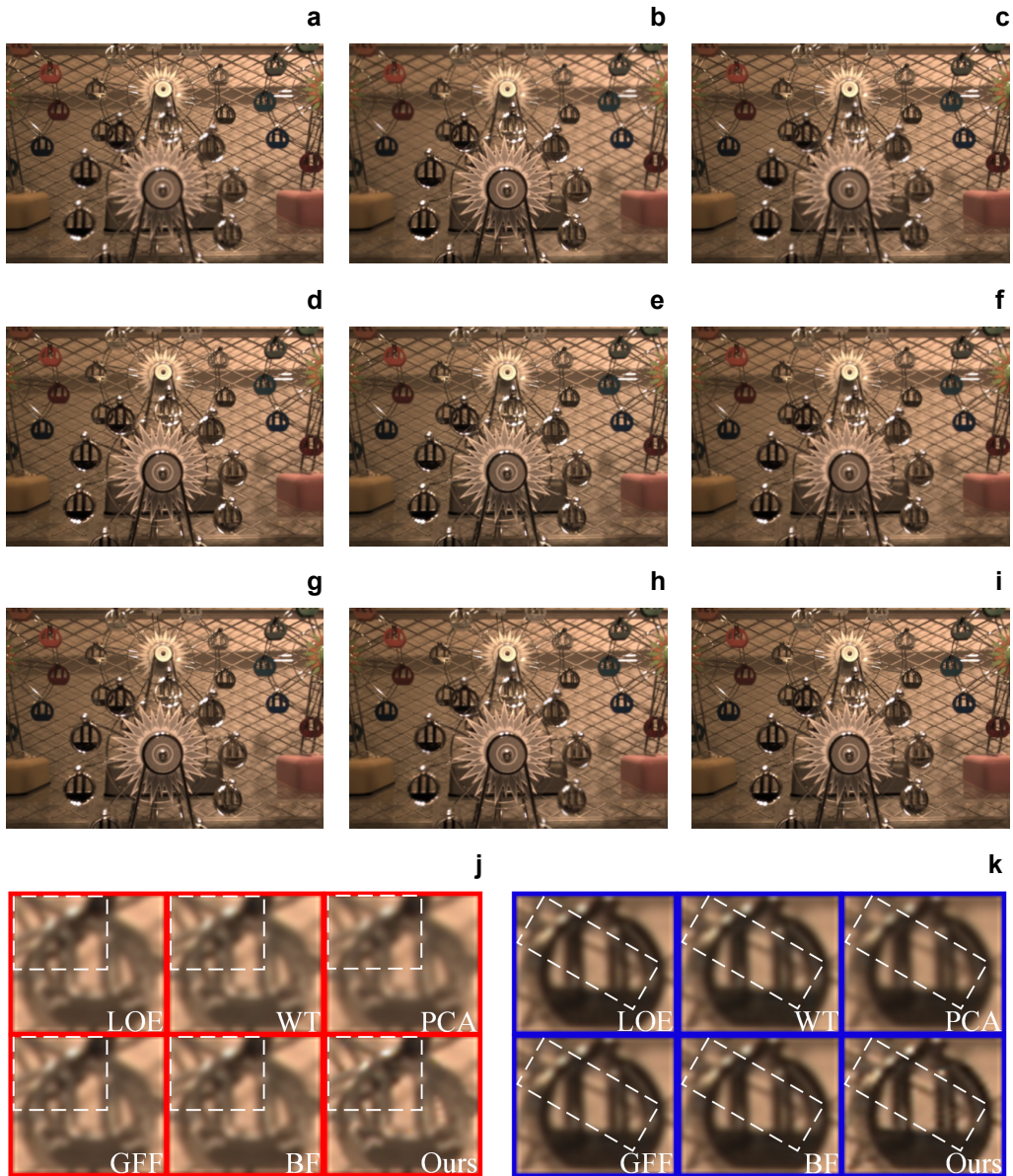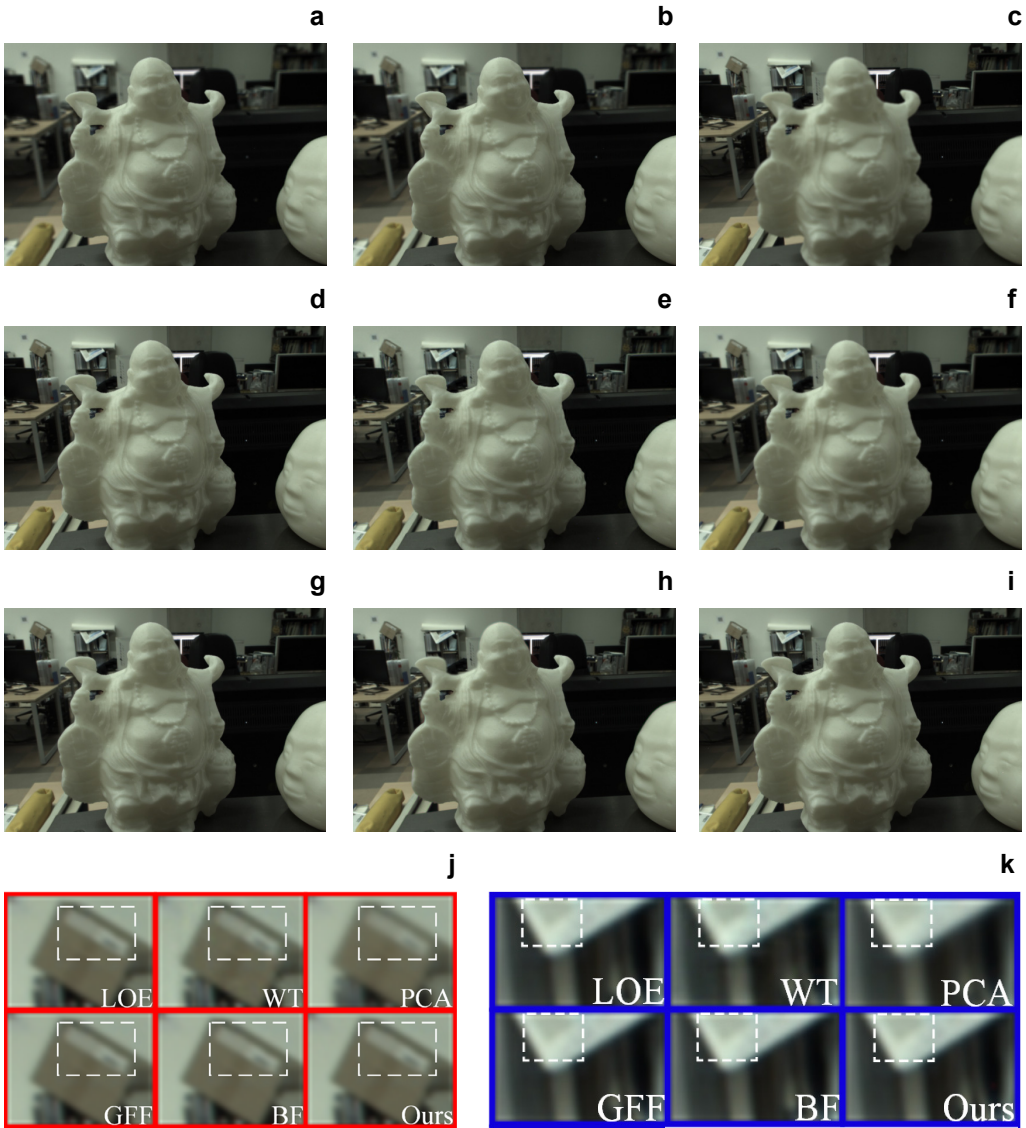
Fig. 5. Comparison of fused image *Wheel*. (**a**) the light field raw image; the refocused image at (**b**) $\alpha_1 =$ = 0.4, and (**c**) $\alpha_2 = 0.85$; (**d**–**i**) the fused image of LOE algorithm, WT algorithm, PCA algorithm, GFF algorithm, BF algorithm and the proposed algorithm respectively; (**j**, **k**) the local magnified areas of the fused images of different algorithms.

evaluated. Since the available light field databases do not give the standard all-in-focus images, three types of widely adopted image quality evaluation metrics are used to evaluate the fused images of different algorithms. They are image feature-based index,

Fig. 6. Comparison of fused image *Buddha*. (**a**) the light field raw image; the refocused image at (**b**) $\alpha_1 =$ 1.0, and (**c**) $\alpha_2 = 5.5$; (**d**–**i**) the fused image of LOE algorithm, WT algorithm, PCA algorithm, GFF algorithm, BF algorithm and the proposed algorithm, respectively; (**j**, **k**) are the local magnified areas of the fused images of different algorithms.

image structure similarity-based index, and human perception inspired index. The feature mutual information (FMI) [20] and phase congruency (PC) [21] belonging to the image feature-based index, the modified structural similarity index (MSSI) [22] belonging to the image structure similarity-based index, and perceptual sharpness of im-

T a b l e. Performance evaluation indices comparison of different fusion algorithms based on *Wheel* image and *Buddha* image.

	Wheel				Buddha			
	FMI	PC	MSSI	PSI	FMI	PC	MSSI	PSI
LOE	0.6880	0.9131	0.9874	0.3260	0.4494	0.8321	0.9768	**0.2542**
WT	0.6733	0.9128	0.9872	**0.3307**	0.4388	0.8253	0.9762	0.2515
PCA	0.6748	**0.9328**	**0.9902**	0.2844	0.4569	**0.8653**	**0.9826**	0.2019
GFF	**0.6898**	0.9167	**0.9884**	0.3157	0.4506	**0.8359**	**0.9827**	0.2391
BF	0.6883	0.9108	0.9876	0.3291	**0.4587**	0.8370	0.9810	0.2501
Ours	**0.6905**	0.9198	0.9862	**0.3406**	**0.4738**	0.8423	0.9822	**0.2767**

age (PSI) [23] belonging to the human perception inspired index are used as the image quality evaluation functions.

The quantitative evaluation results of different algorithms are shown in the Table. Greater value means better performance of the corresponding algorithm. The bold blue value indicates the best value in the corresponding column, and the bold black value indicates the second-best value. The distributions of the best and second best values in the Table verify the advantage of the proposed algorithm. Analyzing the values of different indices in the Table, the proposed algorithm performs best on the FMI and PSI indices and second-best on the PC index. For the MSSI index, even though the proposed algorithm performs worst on the *Wheel* image, the "worst" only reflects in the third decimal place of the evaluation value.

In order to demonstrate the representativeness of the data shown in the Table, ten light field raw images are used to calculate the fused images based on different algorithms. The results of each evaluation index are averaged and the data distribution are given in Fig. 7. By using the proposed algorithm, the fused image quality is best based on the FMI, PC and PSI indices, and third-best based on the MSSI index, which further demonstrates the effectiveness and stability of the proposed algorithm.
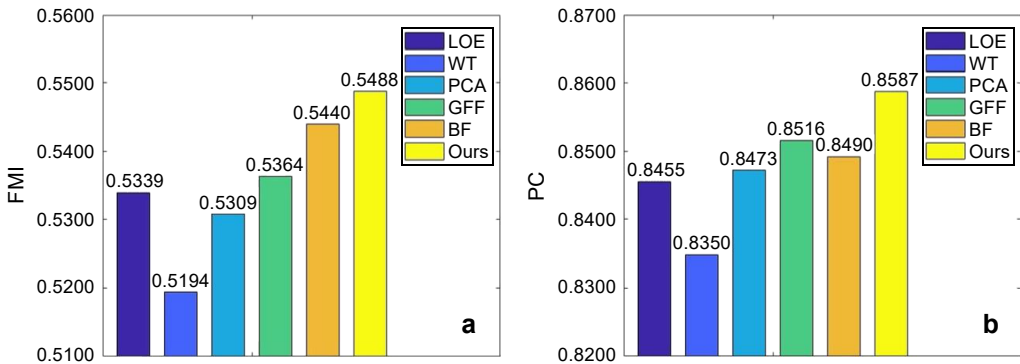
Fig. 7. Average performance evaluation indices comparison of different fusion algorithms: (**a**) the average values distribution of FMI; (**b**) the average values distribution of PC; (**c**) the average values distribution of MSSI; and (**d**) the average values distribution of PSI.
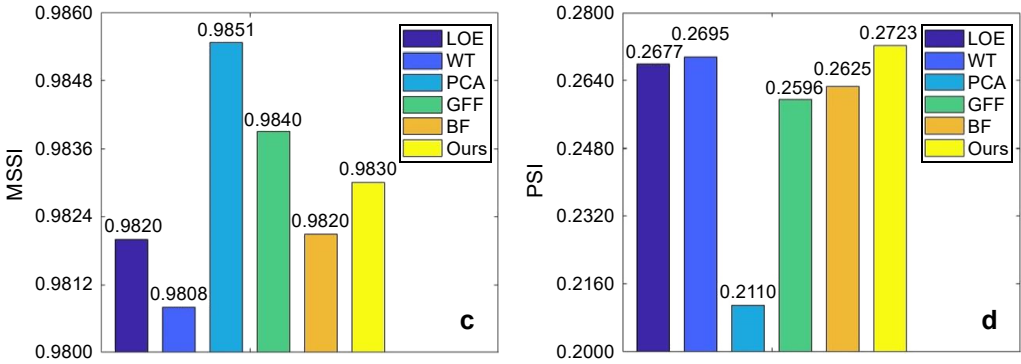
Fig. 7. Continued.

The advantages of the proposed algorithm can be also explained by Fig. 7. Since the 4D light field matrices are directly fused in the proposed method while the 2D refocused images are fused in the other comparison algorithms, the proposed method is more likely to preserve the original information from the source data, resulting in its better performance in the information theory based index FMI. The edge feature is further emphasized by the guided filtering in the proposed algorithm, for which the image feature based index PC is higher in the proposed algorithm. In the proposed method, since the 4D light field matrices are fused directly and then filtered by the central sub-aperture image, the structure of the light field is changed twice, resulting in the declined MSSI index value. The macro-pixel difference function is established based on the intensity perception of human vision in the proposed method, so the human perception inspired index PSI of the proposed method is higher than that of the other algorithms.

5. Conclusions

Different from the traditional light field all-in-focus image acquisition algorithms based on light field spatial information, an all-in-focus image fusion algorithm based on light field angular information is proposed in this paper. Groups of 4D light field matrices corresponding to different focused depths are calculated firstly by changing the basis of the raw 4D light field, then the 4D light field matrices are fused and refined by the guided filtering of the central sub-aperture image, and finally the all-in-focus image is obtained by integrating the refined 4D light field matrix. In the 4D light field matrix fusion, the macro-pixel energy difference caused by the light field angular difference is used to evaluate the sharpness degree and an all-in-focus image can be obtained with higher quality. Experiment results demonstrate the effectiveness and the stability of the proposed algorithm. Quantitative evaluation shows that the proposed algorithm performs best on the information theory-based index and human perception inspired index.

References

[1] DE I., CHANDA B., *Multi-focus image fusion using a morphology-based focus measure in a quad-tree structure*, Information Fusion **14**(2), 2013, pp. 136–146, DOI: 10.1016/j.inffus.2012.01.007.

[2] ZHANG Y., BAI X.Z., WANG T., *Boundary finding based multi-focus image fusion through multi-scale morphological focus-measure*, Information Fusion **35**, 2017, pp. 81–101, DOI: 10.1016/j.inffus.2016.09.006.

[3] WANG D., LIU C., SHEN C., XING Y., WANG Q.H., *Holographic capture and projection system of real object based on tunable zoom lens*, PhotoniX **1**(1), 2020, article 6, DOI: 10.1186/s43074-020-0004-3.

[4] NG R., LEVOY M., BREDIF M., DUVAL G., HOROWITZ M., HANRAHAN P., *Light field photography with a hand-held plenoptic camera*, Stanford University Computer Science Technical Report CSTR 2005-02, 2005, pp. 1–11.

[5] NG R., *Fourier slice photography*, ACM Transactions on Graphics **24**(3), 2005, pp. 735–744, DOI: 10.1145/1073204.1073256.

[6] XIE Y.X., WU Y.C., WANG Y.M., ZHAO X.Y., WANG A.H., *Light field all-in-focus image fusion based on wavelet domain sharpness evaluation*, Journal of Beijing University of Aeronautics and Astronautics **45**(9), 2019, pp. 1848–1854 (in Chinese), DOI: 10.13700/j.bh.1001-5965.2018.0739.

[7] XIAO B., OU G., TANG H., BI X.L., LI W.S., *Multi-focus image fusion by hessian matrix based decomposition*, IEEE Transactions on Multimedia **22**(2), 2020, pp. 285–297, DOI: 10.1109/TMM.2019.2928516.

[8] LI H., WU X.J., *DenseFuse: a fusion approach to infrared and visible images*, IEEE Transactions on Image Processing **28**(5), 2019, pp. 2614–2623, DOI: 10.1109/TIP.2018.2887342.

[9] ZHANG Y.Q., WU J.X., LI H., *Multi-focus image fusion based on similarity characteristics*, Signal Processing **92**, 2019, pp. 1268–1280.

[10] LIU Y., WANG L., CHENG J., LI C., CHEN X., *Multi-focus image fusion: a survey of the state of the art*, Information Fusion **64**, 2020, pp. 71–91, DOI: 10.1016/j.inffus.2020.06.013.

[11] SUN J., HAN Q., KOU L., ZHANG L., ZHANG K., JIN Z., *Multi-focus image fusion algorithm based on Laplacian pyramids*, Journal of the Optical Society of America A **35**(3), 2018, pp. 480–490, DOI: 10.1364/JOSAA.35.000480.

[12] ZOU J.B., SUN W., *Multi-focus image fusion based on lifting stationary wavelet transform and joint structural group sparse representation*, Journal of Computer Applications **38**(3), 2018, pp. 859–865, DOI: 10.11772/j.issn.1001-9081.2017081970.

[13] LI J., SONG M.H., PENG Y.X., *Infrared and visible image fusion based on robust principal component analysis and compressed sensing*, Infrared Physics and Technology **89**, 2018, pp. 129–139, DOI: 10.1016/j.infrared.2018.01.003.

[14] LI S.T., KANG X.D., HU J.W., *Image fusion with guided filtering*, IEEE Transactions on Image Processing **22**(7), 2013, pp. 2864–2875, DOI: 10.1109/TIP.2013.2244222.

[15] FARID M.S., MAHMOOD A., AL-MAADEED S.A., *Multi-focus image fusion using Content Adaptive Blurring*, Information Fusion **45**, 2019, pp. 96–112, DOI: 10.1016/j.inffus.2018.01.009.

[16] QIN X.Q., ZHENG J.Y., HU G., WANG J., *Multi-focus image fusion based on window empirical mode decomposition*, Infrared Physics and Technology **85**, 2017, pp. 251–260, DOI: 10.1016/j.infrared.2017.07.009.

[17] NG R., *Digital Light Field Photography*, PhD Thesis, Stanford University, 2006.

[18] HE K., SUN J., TANG X., *Guided image filtering*, IEEE Transactions on Pattern Analysis and Machine Intelligence **35**(6), 2013, pp. 1397–1409, DOI: 10.1109/TPAMI.2012.213.

[19] YOON Y., JEON H.G., YOO D., LEE J.Y., KWEON I.S., *Light-field image super-resolution using convolutional neural network*, IEEE Signal Processing Letters **24**(6), 2017, pp. 848–852, DOI: 10.1109/LSP.2017.2669333.

[20] HAGHIGHAT M., RAZIAN M A., *Fast-FMI: non-reference image fusion metric*, 2014 IEEE 8th International Conference on Application of Information and Communication Technologies (AICT), 2014, pp. 1–3, DOI: 10.1109/ICAICT.2014.7036000.

[21] ZHAO J., LAGANIERE R., LIU Z., *Performance assessment of combinative pixel-level image fusion based on absolute feature measurement*, International Journal of Innovative Computing, Information & Control **3**(6), 2007, pp. 1433–1447.

[22] YANG C., ZHANG J.Q., WANG X.R., LIU X., *A novel similarity based quality metric for image fusion*, Information Fusion **9**(2), 2008, pp. 156–160, DOI: 10.1016/j.inffus.2006.09.001.

[23] FEICHTENHOFER C., FASSOLD H., SCHALLAUER P., *A perceptual image sharpness metric based on local edge gradient analysis*, IEEE Signal Processing Letters **20**(4), 2013, pp. 379–382, DOI: 10.1109/LSP.2013.2248711.